

Double-illumination photoacoustic microscopy

Junjie Yao,¹ Konstantin I. Maslov,¹ Ernest R. Puckett,¹ Kathryn J. Rowland,²
Brad W. Warner,² and Lihong V. Wang^{1,*}

¹Optical Imaging Laboratory, Department of Biomedical Engineering,
Washington University in St. Louis, St. Louis, Missouri 63130, USA

²Division of Pediatric Surgery, St. Louis Children's Hospital, Department of Surgery,
Washington University School of Medicine, St. Louis, Missouri 63110, USA

*Corresponding author: lhwang@biomed.wustl.edu

Received November 15, 2011; accepted January 7, 2012;
posted January 10, 2012 (Doc. ID 158148); published February 13, 2012

Recent developments of optical-resolution photoacoustic microscopy (OR-PAM) have improved its spatial resolution and imaging speed. However, the penetration depth of OR-PAM is still limited to ~ 1 mm in tissue, owing to the strong tissue scattering. Here, we have developed double-illumination PAM (DI-PAM), which illuminates the sample from both top and bottom sides simultaneously. Through phantom and *in vivo* experiments, we have demonstrated for thin targets that DI-PAM has a penetration depth of ~ 2 mm in tissue at 532 nm and a focal zone of $260 \mu\text{m}$, both significant improvements over traditional reflection or transmission-mode OR-PAM. © 2012 Optical Society of America

OCIS codes: 180.0180, 110.5120, 150.2945.

Taking advantage of rich optical absorption contrast and weak ultrasonic scattering in tissue, photoacoustic microscopy (PAM) has proved to be capable of anatomical, functional, and molecular imaging, with highly scalable spatial resolution, penetration depth, and imaging speed [1–5]. Based on the confocal configuration of the optical illumination and acoustic detection, PAM can be classified into acoustic-resolution PAM (AR-PAM) and optical-resolution PAM (OR-PAM). While AR-PAM has achieved so far tens of micrometers resolution with a penetration depth up to 3 mm in tissue [6], OR-PAM focuses on superficial imaging with at least capillary level resolution [1]. Recently, the imaging performance of OR-PAM has been significantly improved in terms of spatial resolution and imaging speed. By using a water-immersion optical objective with a 1.23 numerical aperture (NA), a 220 nm lateral resolution at 532 nm wavelength has been achieved [7]. Meanwhile, by using a fast voice-coil scanner, the sectional imaging speed of OR-PAM has been pushed to 40 Hz over a 1 mm range [8]. Despite the previously described improvements, the penetration depth of OR-PAM is still restricted to one transport mean-free path (~ 1 mm in tissue), owing to the strong optical scattering in tissue. Moreover, the strong absorption of hemoglobin in the visible spectral range further reduces the $1/e$ penetration depth to less than $50 \mu\text{m}$ in blood vessels, which may cause shallower vessels to shadow deeper vessels. This penetration limitation applies to both reflection-mode and transmission-mode OR-PAM. Only a layer of tissue on the optical illumination can be imaged [2,3,7]. By illuminating light from both the top and bottom sides of the sample, we have developed a double-illumination PAM (DI-PAM) to improve the penetration depth to ~ 2 mm in thin biological tissue. At the same time, the optical focal zone is expanded to $\sim 260 \mu\text{m}$.

In DI-PAM (Fig. 1), a Nd:YVO₄ laser (Elforlight, SPOT) generates 1.5 ns pulses at a 532 nm wavelength. The pulses are reshaped by an iris (ID25SS, Thorlabs) and attenuated by a neutral density filter (NDC-50C-2M,

Thorlabs). The attenuated beam is then split into two subbeams (top and bottom) by a 50/50 beam splitter (BSW04, Thorlabs). The top beam is focused by a condenser lens (LA1131, Thorlabs) before passing through a $50 \mu\text{m}$ pinhole (P50C, Thorlabs) for further spatial filtering. The filtered beam is then focused by an optical objective (AC127-050-A, Thorlabs; NA: 0.1 in air) into the sample from the top. A beam combiner composed of a thin layer of silicone oil sandwiched by a right-angle prism (NT32-545, EdmundOptics) and a rhomboid prism (NT49-419, EdmundOptics) provides acoustic-optical coaxial alignment. The resultant photoacoustic waves are detected by an ultrasonic transducer (V214-BB-RM, Olympus-NDT) with a central frequency of 50 MHz. An acoustic lens with an NA of 0.5 is ground into the bottom of the rhomboid prism to provide an acoustic focal diameter of $30 \mu\text{m}$. An optical correction lens is attached to the top of the beam combiner to correct the aberration. The acoustic lens is submerged in a water tank for ultrasound

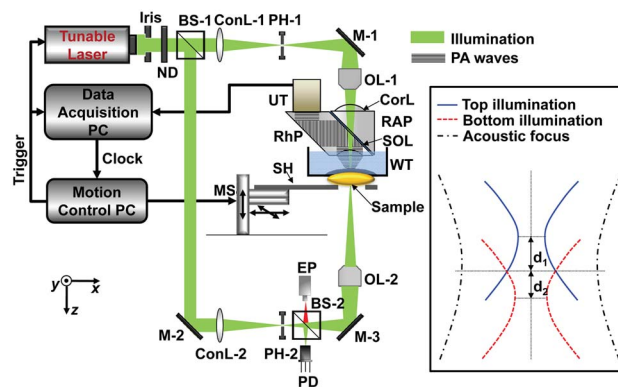


Fig. 1. (Color online) Schematic of DI-PAM. $d_{1,2}$; Rayleigh range. ND, neutral density filter; BS, beam splitter; ConL, condenser lens; PH, pinhole; M, mirror; OL, objective lens; CorL, correction lens; RAP, right-angle prism; SOL, silicone oil layer; RhP, rhomboid prism; UT, ultrasonic transducer; WT, water tank; SH, sample holder; MS, motor scanner; EP, eyepiece; PD, photodiode.

coupling. The bottom beam duplicates the same path as the top beam, except that it is directly focused into the sample from the bottom without going through the beam combiner and water tank. As shown in the inset of Fig. 1, by carefully adjusting the positions of two objectives, we achieved a coaxial configuration of the two optical foci and the acoustic focus. To best expand the optical focal zone, the top and bottom optical foci are both approximately one Rayleigh range apart from the acoustic focus. Volumetric imaging is acquired by two-dimensional raster scanning of the sample. An eyepiece is added to the bottom beam path to view the imaging region through the reverse path of the illumination. A photodiode is also added to monitor the fluctuations of the laser pulse intensity.

To measure the lateral resolution of the DI-PAM system, a sharp ink edge was imaged in water at varied depths while the optical focus was fixed. From the edge spread function, the full width half maximum of the line spread function was computed to determine the lateral resolution. As a comparison, the lateral resolution under either top or bottom illumination was also quantified using the same protocol. The measured results were fitted using the theoretical model for a Gaussian beam

$$w(z) = \sqrt{w_0^2 + \left[\frac{\lambda(z - z_0)}{\pi w_0} \right]^2},$$

where $w(z)$ is the lateral resolution at depth z , w_0 is the focal diameter, λ is the wavelength, and z_0 is the focal depth. While λ is known, w_0 and z_0 are the unknown parameters to fit for. As shown in Fig. 2(a), the top illumination gives a focal diameter of $2.3 \mu\text{m}$ with a focal zone of $100 \mu\text{m}$. Here, focal zone is defined as the range of depths over which the system maintains a lateral resolution no worse than $\sqrt{2}w_0$. Similarly, the bottom illumination gives a focal diameter of $2.9 \mu\text{m}$, with a focal zone of $170 \mu\text{m}$. The two foci are $160 \mu\text{m}$ apart. The top illumination has a tighter focusing owing to the addition of the

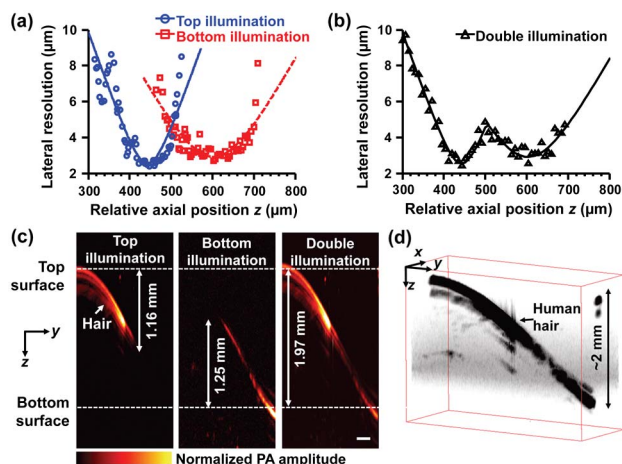


Fig. 2. (Color online) System characterization of DI-PAM. (a), (b) Lateral resolution as a function of the axial position relative to the starting depth of data acquisition, under top, bottom, and double illuminations, respectively. Solid curves: theoretical fitting. (c) Side-view DI-PAM images of the human hair inside the chicken tissue under three illuminations. Scale bar: $200 \mu\text{m}$. (d) Volumetric rendering of the human hair imaged by DI-PAM.

correction lens, which gives an effective NA of 0.133 in water, while the bottom illumination has an NA of 0.1 in air. As can be seen in Fig. 2(b), under double illumination, the lateral resolution has a “W” shape distribution along the depth, which is determined by the overall light intensity of the two beams. The two valleys of the “W” distribution are $2.3 \mu\text{m}$ and $2.9 \mu\text{m}$ in lateral resolution, which equal the top and bottom focal diameters, respectively. The effective focal zone is expanded to $260 \mu\text{m}$, which is the sum of the focal zones of the two valleys ($100 \mu\text{m}$ and $160 \mu\text{m}$, respectively). Thus, by increasing the focal zone by $160 \mu\text{m}$ over the top illumination or $90 \mu\text{m}$ over the bottom illumination, DI-PAM maintains the lateral resolution over a longer depth range.

To measure the penetration depth of the DI-PAM system, a black human hair was obliquely embedded in a 2-mm-thick piece of fresh chicken breast tissue. The two ends of the hair tightly pressed against the top and bottom surfaces of the tissue and served as landmarks of the tissue boundaries. The top and bottom illuminations both had a pulse energy of 80 nJ. As shown in Fig. 2(c), while either single illumination can image only the top (1.16 mm) or bottom (1.25 mm) part of the hair, DI-PAM can clearly image the whole hair [Fig. 2(d)], demonstrating a penetration depth of at least $\sim 2 \text{ mm}$ in biological tissue.

The improved system performance enables DI-PAM to image deeper vasculature while maintaining capillary-level lateral resolution. All experimental procedures were carried out in conformity with the protocol approved by the Animal Studies Committee at Washington

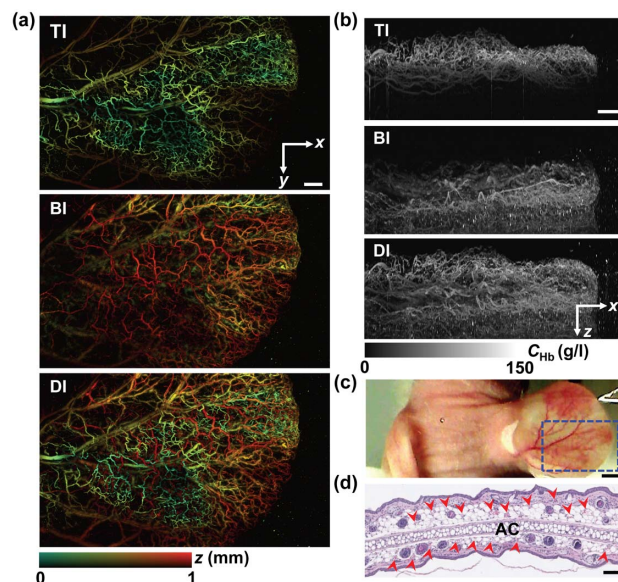


Fig. 3. (Color online) DI-PAM of mouse ear *in vivo*. (a) Top-view depth-encoded DI-PAM images of the right ear of a nude mouse bearing a U87 glioblastoma tumor, under top (TI), bottom (BI), and double (DI) illuminations, respectively. z is coded in colors. Scale bar: $500 \mu\text{m}$. (b) Side-view DI-PAM images under three illuminations. C_{Hb} , total hemoglobin concentration. Scale bar: $500 \mu\text{m}$. (c) Photograph of the mouse ear. The imaged area is indicated by the blue dashed box. Scale bar: 2 mm. (d) Histology image of hematoxylin and eosin (H&E) stained tissue slice across the mouse ear. AC; auricular cartilage. Arrowheads: blood vessels. Scale bar: $100 \mu\text{m}$.

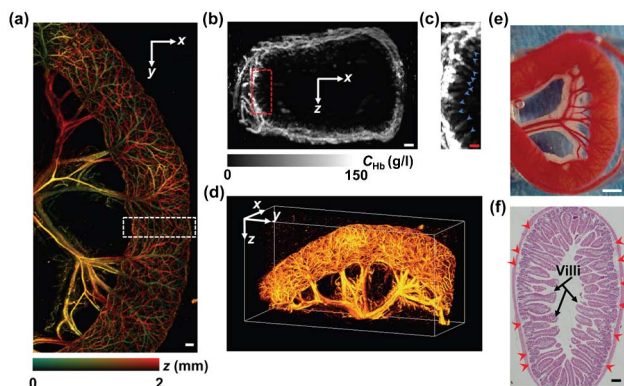


Fig. 4. (Color online) DI-PAM of the small intestine of a C57BL/6 mouse *in vivo*. (a) Top-view depth-encoded DI-PAM image of the small intestine under double illumination. Scale bar: 500 μm . (b) Side-view DI-PAM image of the region indicated by the dashed box in (a). C_{Hb} , total hemoglobin concentration. Scale bar: 250 μm . (c) Close-up of the small region indicated by the dashed box in (b). The intestinal villi are indicated by the arrowheads. Scale bar: 100 μm . (d) Volumetric rendering of the small intestine imaged by DI-PAM. (e) Photograph of the small intestine after surgical exposure. Scale bar: 1 mm. (f) Histology image of H&E stained cross section of the small intestine. Arrowheads: blood vessels. Scale bar: 200 μm .

University in St. Louis, Missouri. The mouse ear was chosen for a first demonstration. The ear of a 12-week-old nude mouse (Hsd:Athymic Nude-Foxn1NU, Harlan) is composed of a layer of auricular cartilage sandwiched by two layers of skin tissue [Fig. 3(d)]. To increase the mouse ear thickness, we injected $\sim 10^6$ U87 glioblastoma cells into the ear [Fig. 3(c)]. A $10 \times 15 \text{ mm}^2$ area including the tumor region was sequentially imaged under top, bottom, and double illuminations 7 days after the tumor cell injection. In Fig. 3(a), the depth-encoded maximum amplitude projection (MAP) images show that only the top layer vessels or bottom layer vessels can be well imaged under top or bottom illumination, respectively. Optical shadowing is the key reason. Although some big vessels from the other layer are discernible, they are very much blurred because of the degraded lateral resolution. In contrast, DI-PAM can clearly image both layers of vasculature without shadowing or blurring. The side-view MAP images in Fig. 3(b) further demonstrate the improvements of DI-PAM in penetration depth and focal zone, imaging through the whole ear with a thickness more than 1 mm.

In a second demonstration of DI-PAM, we imaged the vascular network surrounding the small intestine of a living black mouse (C57BL/6Hsd, Harlan). After surgical exposure, part of the small intestine was gently pulled out and placed on the sample holder for DI-PAM imaging. The high vessel density on one side of the intestine would prevent imaging the other side by single-illumination PAM systems [Figs. 4(e)–4(f)]. In contrast, DI-PAM can obtain complete cross-sectional images of the intestine that is close to 2 mm in diameter [Figs. 4(a)–4(b)]. The depth-encoded MAP image shows a dense mesenteric vascular network, where the vessels from the top side the bottom side were shown in different colors [Fig. 4(a)]. The side-view MAP image of the section indicated by the dashed box in Fig. 4(a) appears to be a

closed loop [Fig. 4(b)]. The villi on the lumen of the intestine are also clearly resolved [Fig. 4(c)].

Simply doubling the incident light intensity for single illumination OR-PAM can also increase the penetration depth. However, the resultant improvement is not equivalent to that provided by DI-PAM. First, doubling incident light will not result in doubling of the penetration depth, since the attenuation of light by tissue is exponential rather than linear. Second, in DI-PAM, the light intensity on the tissue surface was 22 mJ/cm^2 for both top and bottom illuminations, which is still close to the American National Standards Institute (ANSI) safety limit (20 mJ/cm^2 in the visible spectral region). However, simply doubling the light intensity for single illumination (44 mJ/cm^2) will break the ANSI limit and thus increase the risk of damaging tissue.

The focal zone of single illumination OR-PAM can also be expanded by depth scanning and stacking the data sets together. However, this is not equivalent to the improvement owing to DI-PAM. First, strong tissue scattering would degrade the lateral resolution as the focal position deepens. Second, the imaging time would be increased by depth scanning. In contrast, DI-PAM expands the focal zone without sacrificing lateral resolution and imaging speed.

In conclusion, we have developed double-illumination PAM, which offers improved penetration depth and expanded focal zone. Compared with traditional reflection or transmission-mode OR-PAM, the penetration depth has been improved to at least 2 mm in thin biological tissue. In addition, the focal zone has been improved to 260 μm , with a lateral resolution no worse than 4 μm . Deep microscopy of microvascular anatomy in a mouse ear and small intestine was performed. Although not demonstrated here, DI-PAM is intrinsically ready for label-free measurements of oxygen saturation, blood flow, and oxygen metabolism.

The authors appreciate Prof. James Ballard's close reading of the manuscript and thank Yan Liu and Joon-Mo Yang for useful discussion and technical assistance. This work was sponsored by National Institutes of Health (NIH) grants R01 EB000712, R01 EB008085, R01 CA134539, U54 CA136398, R01 CA157277, R01 CA159959, and 5P60 DK02057933. Lihong Wang has a financial interest in Microphotoacoustics, Inc., and Endra, Inc., which, however, did not support this work.

References

1. J. Yao and L. V. Wang, *Contrast Media Mol. Imaging* **6**, 332 (2011).
2. K. Maslov, H. F. Zhang, S. Hu, and L. V. Wang, *Opt. Lett.* **33**, 929 (2008).
3. Z. X. Xie, S. L. Jiao, H. F. Zhang, and C. A. Puliafito, *Opt. Lett.* **34**, 1771 (2009).
4. P. Hajireza, W. Shi, and R. J. Zemp, *Opt. Lett.* **36**, 4107 (2011).
5. J. Yao, K. I. Maslov, Y. Zhang, Y. Xia, and L. V. Wang, *J. Biomed. Opt.* **16**, 076003 (2011).
6. H. F. Zhang, K. Maslov, G. Stoica, and L. H. V. Wang, *Nat. Biotechnol.* **24**, 848 (2006).
7. C. Zhang, K. Maslov, and L. V. Wang, *Opt. Lett.* **35**, 3195 (2010).
8. L. Wang, K. Maslov, J. Yao, B. Rao, and L. V. Wang, *Opt. Lett.* **36**, 139 (2011).